J. Fluid Mech. (2002), *vol.* 469, *pp.* 343–367.
DOI: 10.1017/S0022112002002045 Printed in the United Kingdom

A local nonlinear solution as an approximation to low-frequency spanwise jitter in thermoconvective flows

By P. GRASSIA[1] AND D. RICHARDSON[2]

[1]Department of Chemical Engineering, UMIST, PO Box 88, Manchester M60 1QD, UK

[2]Department of Mathematics, University of Manchester, Oxford Rd, Manchester M13 9PL, UK

(Received 12 February 2001 and in revised form 20 June 2002)

A shallow fluid-filled cavity with a longitudinal applied temperature gradient is subjected to spanwise accelerations (g-jitter) representing the space-based microgravity environment. A simplified slot model is introduced to describe the buoyancy-driven flow and advected temperature fields produced in the cavity. Numerical solutions indicate that boundary layer behaviour can manifest itself in the limit of strong g-jitter (large Rayleigh number Ra). However, boundary layer thicknesses do not obey the conventional $Ra^{-1/4}$ scaling that typically arises in free thermal convection problems. This anomalous scaling results from the three-dimensional complexity of the flow and advected temperature fields, which are not themselves produced by a single fixed applied temperature change. Three different regimes are identified at large Rayleigh number characterized by the shapes of the advected temperature profiles. These regimes are selected according to the values of the Biot number Bi and an aspect ratio parameter. Simple models are presented of the boundary layer behaviour which reproduce, in each regime, the numerically predicted scalings for boundary layer thickness and advected temperature. These models give a succinct overall picture of the slot behaviour in the buoyancy-dominated limit.

1. Introduction

The launch of the International Space Station in 1998† suggests that engineers of the future may be routinely processing materials in space. This possibility has presented the scientific challenge to understand better the space-based microgravity environment (Alexander 1990; Nelson 1991; Thomson, Drolet & Viñals 1996; Alexander *et al.* 1996). Orbiting spacecraft are subject to residual accelerations, called g-jitter, which are generally time dependent (periodic or random or a mixture of both), and which can act in various directions. The fluid mechanicist can contribute to the scientific discussion, since g-jitter produces novel fluid motions, e.g. in processing a crystal melt, which would not occur in the fixed-gravity environment of Earth (Gresho & Sani 1970; Kamotani, Prasad & Ostrach 1981; Ostrach 1982; Gershuni & Zhukhovitskiy 1986; Gershuni *et al.* 1989; Wadih & Roux 1988; Biringen & Danabasoglu 1989, 1990; Biringen & Peltier 1990; Shen *et al.* 1990; Neitzel *et al.* 1991, 1993; Thévenard & Ben Hadid 1991; Saunders *et al.* 1992; Farooq & Homsy 1994; Kondos & Subramanian 1996; Lizée & Alexander 1997; Suresh, Christov & Homsy 1999).

† See http://spaceflight.nasa.gov/station/assembly for information on the status of the International Space Station project.

One class of models which rewards study fruitfully is that of so-called slot models (Elder 1965; Gill 1966; Gill & Davey 1969; Gill & Kirkham 1970; Bergholz 1978; Sen & Davis 1982; Smith & Davis 1983*a*, *b*; Farooq & Homsy 1996; Grassia & Homsy 1998*a*). It is a feature of such models that the geometry of the fluid system is idealized, typically by considering a fluid layer of infinite extent in two directions, but of finite depth in the third. This geometric simplification can make slot models both simple and fast to handle numerically: indeed sometimes they are even analytically tractable. In spite of the simple geometry, all the key fluid physics one might hope to describe (inertia, buoyancy, viscosity, thermal conduction and convection) is retained. Thus one can focus clearly on the physics without being concerned that an effect one observes might be solely dependent on some geometric peculiarity.

Most slot models to date have been confined to two-dimensional flow fields. However a recent study has extended this class of models to three dimensions (Grassia & Homsy 1998*b*, *c*). The problem considered was a shallow fluid layer with a uniform temperature gradient applied along its length, and with g-jitter also imposed along the layer, but perpendicular to the applied temperature gradient, i.e. the applied jitter was spanwise. Buoyant forces produced a circulation, ultimately leading to a three-dimensional pattern of flow and advected temperature fields. These fields had well-identified structure in both directions along the fluid layer, but the challenge was to determine their quite complicated variation across the layer. This calculation was only tackled in the limit of weak applied jitter (low Rayleigh number Ra) where a perturbation expansion could be used.

The purpose of the present paper is to extend the results of Grassia & Homsy (1998*b*, *c*) to the case of finite-amplitude jitter. Numerical techniques must be used. However, a purely numerical study is not our sole objective here. We also want to extract the asymptotic behaviour of the slot model in the limit of large Rayleigh number Ra. It is well-known in fluid mechanics problems involving some dimensionless parameter, such as Reynolds, Péclet or Rayleigh numbers, that when the governing dimensionless parameter becomes large, boundary layer behaviour is observed (Batchelor 1967; Leal 1992). The boundary layer thickness scales as a power law function of the governing dimensionless parameter, and the exponent of the power law characterizes the particular type of boundary layer. Knowing these layer thicknesses is of more than academic interest, since they indicate where and how much one needs to refine a numerical mesh when solving a real problem in a complex geometry.

In free convection problems, layer thicknesses which scale like $Ra^{-1/4}$ are commonly found (Farooq & Homsy 1994; Elder 1965; Gill 1966; Gill & Davey 1969; Bergholz 1978; Farooq & Homsy 1996; Grassia & Homsy 1998*b*, *c*). However, this scaling applies to layers produced in response to a known imposed temperature difference. This is not the case for the three-dimensional slot model that we propose to study here. Instead there are multiple flow and advected temperature fields to be considered. One component of the flow may produce an advected temperature, which may in turn produce further components of both the flow and temperature fields. Thus the temperature change is coupled to the flow, not imposed from without. As we shall see, it is quite a challenge to extract the correct boundary layer behaviour from the governing equations. Nonetheless it is a worthwhile task, because it produces a simple picture of the slot behaviour in the buoyancy-dominated limit.

The structure of the paper is as follows. In the next section we introduce the slot model and its governing equations. Then we present the numerical solutions over a range of parameter values. Next we tackle the models for the boundary layer

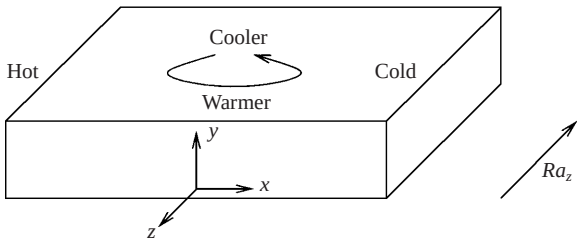

FIGURE 1. A shallow cavity of unit depth has a unit temperature gradient applied along its length and is subjected to low-frequency, spanwise jitter characterized by an instantaneous Rayleigh number Ra_z. A circulation is established which advects heat, producing spanwise as well as lengthwise temperature gradients.

behaviour of the slot in the large Rayleigh number Ra limit. Finally we discuss the numerical results in the light of the boundary layer model and offer conclusions. A far more detailed discussion of the work that we present can be found in Richardson (1999).

2. The buoyant slot

The physical problem to be considered and the associated governing equations have already been developed in the literature (Grassia & Homsy 1998*b*, *c*). We shall review the rudiments of the development here. We adopt a dimensionless formulation throughout: the relation between this dimensionless notation and its dimensional counterpart is explained in the Appendix.

A shallow cavity of unit depth (see figure 1) is oriented along the y-axis of an xyz coordinate system with the origin located at the centre of the cavity's base. The cavity is filled with a fluid of Prandtl number Pr, and a unit temperature gradient is applied along it (x-direction). Thermal buoyancy forces are present. Spanwise (z-direction) g-jitter is applied. As in previous studies (Grassia & Homsy 1998*a*, *b*, *c*) this is assumed to be at low frequency (quasi-static), so that we are only concerned with the instantaneous value of the applied acceleration: this is conveniently represented by a (spanwise) Rayleigh number Ra_z.

The base of the cavity $y = 0$ is assumed to be thermally insulated, and no-fluid-penetration and no-slip conditions apply there. The top surface of the fluid at $y = 1$ can exchange heat with the outside environment (heat transfer coefficient represented by a Biot number Bi). This surface is also assumed to remain flat (valid if surface tension forces are strong enough) and it cannot support tangential stresses (Marangoni forces are ignored).

As is explained elsewhere (Grassia & Homsy 1998*b*, *c*) the temperature gradient and applied acceleration couple to produce vertical vorticity and hence a circulation flow around the cavity. However, this flow does not exist in isolation: it also advects temperature, leading thereby to more vorticity production and additional flows. A complicated three-dimensional pattern of flow and temperature fields results. While it is feasible to compute numerically these fields for particular parameter values, e.g. by adopting numerical techniques recently deployed for related problems (Or & Kelly 1998; Chen & Chen 1999; Christov & Homsy 2001; Skarda 2001), our objective is to replace the true shallow cavity by a geometrically simpler slot model. This will lead to a more mathematically tractable system, enabling a comprehensive investigation of parameter space.

The governing continuity, momentum and thermal equations in the quasi-static limit are

$$\nabla \cdot \boldsymbol{u} = 0, \tag{2.1}$$

$$\frac{1}{Pr}(\boldsymbol{u} \cdot \nabla)\boldsymbol{u} = -\nabla p + \nabla^2 \boldsymbol{u} + Ra_z \boldsymbol{e}_z T, \tag{2.2}$$

$$\boldsymbol{u} \cdot \nabla T = \nabla^2 T, \tag{2.3}$$

where $\boldsymbol{e}_z$ is the unit vector in the z-direction, and we have adopted the sign convention (Grassia & Homsy 1998*a*, *b*) that positive Ra_z corresponds to effective gravity in the negative $\boldsymbol{e}_z$-direction. The boundary conditions (defining temperature to be the sum of an applied field and an advected part arising due to the flow, $T \equiv -x + T^{advected}$) are

$$\boldsymbol{u} = T^{advected}_{,y} = 0 \qquad \text{at} \qquad y = 0, \tag{2.4}$$

$$u_{,y} = v = w_{,y} = T^{advected}_{,y} + BiT^{advected} = 0 \qquad \text{at} \qquad y = 1. \tag{2.5}$$

The environment above the slot is assumed to be held at the value of the applied temperature field, so that the advected field alone determines heat transfer at the top boundary.

2.1. *Local solution in a central fluid patch*

The general solutions of equations (2.1)–(2.5) are complicated fully three-dimensional functions. For a *shallow* fluid-filled cavity, we propose a so-called local solution, which has an assumed simple functional form in the x- and z-directions, but makes no assumptions across the y-direction. Such a local solution constitutes our slot analogue of the true cavity. It makes no attempt to satisfy lateral boundary conditions, and hence can only be valid over a small fraction of the length and breadth of the actual cavity: this may nonetheless still correspond to many times the cavity depth in view of the shallowness assumption. The physical interpretation is that we are looking at a central patch of fluid located in the neighbourhood of $x = z = 0$. Employing the notation used by other studies (Grassia & Homsy 1998*c*, *a*; Richardson 1999), we propose for velocity components u, v and w, pressure p and advected temperature $T^{advected}$

$$u \approx xu_{10}(y) + zu_{01}(y), \tag{2.6}$$

$$v \approx v_{00}(y), \tag{2.7}$$

$$w \approx xw_{10}(y) + zw_{01}(y), \tag{2.8}$$

$$p \approx p_{00}(y) + \tfrac{1}{2}x^2 p_{20} + \tfrac{1}{2}z^2 p_{02} + xzp_{11}, \tag{2.9}$$

$$T^{advected} \approx xT_{10}(y) + zT_{01}(y). \tag{2.10}$$

Equations (2.6) and (2.8) have simple, i.e. linear, dependence in x and z, compatible with the (reflectional) symmetries of equations (2.1)–(2.5). The velocity fields $zu_{01}(y)$ and $xw_{10}(y)$ represent circulations about the central point of the slot, whereas $xu_{10}(y)$ and $zw_{01}(y)$ represent inflows toward or outflows away from the centre. Meanwhile $v_{00}(y)$ corresponds to the vertical funnelling of fluid: the lack of any x or z dependence here is dictated by equation (2.1). The pressure field must have the form shown in equation (2.9) to enable it to have gradients in all the necessary directions. It should be noted that p_{20}, p_{02} and p_{11} are constants, independent of y. The term involving p_{20} appears in the x momentum equation, that involving p_{02} appears in the z momentum

equation, whereas the p_{11} term appears in both equations, and couples them. The function $p_{00}(y)$ is required only to balance the y momentum equation: it turns out to have no dynamical significance (Grassia & Homsy 1998*b*, *c*; Richardson 1999). For the advected temperature in equation (2.10) there is again a simple linear dependence in x and z, consistent with the symmetries of equations (2.1)–(2.5). The fields $xT_{10}(y)$ and $zT_{01}(y)$ respectively modify the lengthwise temperature gradient, and introduce spanwise gradients.

What we shall typically find is that the lengthwise-varying part $xT_{10}(y)$ of the advected temperature tends to oppose the applied field, and at large Ra_z nearly cancels it: the total gradient (applied plus convected) is therefore small. The physical implication for a true shallow cavity, with a fixed temperature difference say applied across its length between two sidewalls, is as follows. Recall that the local solution models the shallow cavity near its centre and far from any sidewalls. Thus for a real shallow cavity, any large total lengthwise temperature gradients will be confined near the sidewalls. Analogous behaviour is seen at large Rayleigh number in a much simpler (two-dimensional) convective flow problem, i.e. a temperature difference applied horizontally across the thickness of a vertically aligned slot, with vertical gravity: the effect of convection is to confine large total horizontal temperature gradients to the sidewalls (Elder 1965; Gill 1966; Gill & Davey 1969; Bergholz 1978; Farooq & Homsy 1994, 1996).

Before proceeding with our local solution, we shall take the limit $Pr \to \infty$, which will apply throughout the remainder of the paper. This serves to reduce the size of the parameter space which the local solutions must explore. When $Pr \to \infty$, we are considering buoyancy-dominated, viscous-limited flows, but not how such flows are modified by inertia (see equation (2.2)). Earlier studies have found that solutions (at least for small Ra_z) were extremely insensitive to Prandtl number, in the sense that $Pr \to \infty$ and $Pr = 1$ results were virtually identical (Grassia & Homsy 1998*b*, *c*). Some crystallization problems, e.g. involving molten metals, do however exhibit Prandtl numbers much smaller than unity (Braunsfurth & Mullin 1996; Braunsfurth *et al.* 1997): neglect of inertia may be invalid in such cases.

2.2. *Governing equations for the local solution*

We can now supply the equations governing the slot behaviour. We shall see that these need to be supplemented by a number of closure relations, which we shall discuss briefly. The latter relations determine the extent that the central fluid patch described by the local solution exchanges mass with the rest of the cavity.

If equations (2.6)–(2.10) are substituted into (2.1)–(2.5) with $Pr \to \infty$, and then terms with corresponding powers of x and z are collected, we obtain

$$u_{10} + v_{00,y} + w_{01} = 0, \tag{2.11}$$

$$0 = -p_{20} + u_{10,yy}, \tag{2.12}$$

$$0 = -p_{11} + u_{01,yy}, \tag{2.13}$$

$$0 = -p_{11} + w_{10,yy} + Ra_z(T_{10} - 1), \tag{2.14}$$

$$0 = -p_{02} + w_{01,yy} + Ra_z T_{01}, \tag{2.15}$$

$$u_{10}(T_{10} - 1) + v_{00}T_{10,y} + w_{10}T_{01} = T_{10,yy}, \tag{2.16}$$

$$u_{01}(T_{10} - 1) + v_{00}T_{01,y} + w_{01}T_{01} = T_{01,yy}, \tag{2.17}$$

along with boundary conditions

$$u_{10} = u_{01} = v_{00} = w_{10} = w_{01} = T_{10,y} = T_{01,y} = 0 \qquad \text{at} \qquad y = 0, \tag{2.18}$$

$$u_{10,y} = u_{01,y} = w_{10,y} = w_{01,y} = T_{10,y} + BiT_{10} = T_{01,y} + BiT_{01} = 0 \qquad \text{at} \qquad y = 1. \tag{2.19}$$

In the above, (2.11) is a continuity equation, equations (2.12)–(2.13) represent x momentum, equations (2.14)–(2.15) represent z momentum, and (2.16)–(2.17) are thermal equations. Note that the y momentum equation is not reported here since it has no dynamical significance (Grassia & Homsy 1998*b*, *c*; Richardson 1999). Likewise note that in boundary conditions (2.18)–(2.19) only one condition on vertical velocity is needed (Grassia & Homsy 1998*b*, *c*), as we would expect for first-order equation (2.11).

Equations (2.11)–(2.19) are supplemented by the following closure relations. For the circulation part of the flow given by $zu_{01}(y)$ and $xw_{10}(y)$, we define, as in previous work (Grassia & Homsy 1998*b*, *c*), a parameter A_{zx} which represents the spanwise-to-lengthwise aspect ratio of the central fluid patch. We assume that none of the circulation flow will leak out of the patch into the surroundings. In other words we assume that the depth-averaged circulation flux crossing the lengthwise axis between the central point and some arbitrary x matches that crossing the spanwise axis between the central point and $z = A_{zx}x$. This implies

$$\int_0^1 w_{10}\,\mathrm{d}y + A_{zx}^2 \int_0^1 u_{01}\,\mathrm{d}y = 0. \tag{2.20}$$

Thus A_{zx} becomes a key parameter in the model: it can be thought of as the spanwise-to-lengthwise wavelength ratio for the slot flow and temperature fields.

Closure assumptions for the inflow–outflow components of the velocity field $xu_{10}(y)$ and $zw_{01}(y)$, suppose that, in the depth average, there is no net pumping of fluid in from one direction (e.g. along the x-axis), and no net pumping out in the transverse direction (e.g. along the z-axis). Hence

$$\int_0^1 u_{10}\,\mathrm{d}y = \int_0^1 w_{01}\,\mathrm{d}y = 0, \tag{2.21}$$

meaning that both u_{10} and w_{01} are so-called return flows (Sen & Davis 1982; Smith & Davis 1983*a*).

We emphasize that the integral conditions (2.20)–(2.21) are nothing more than plausible closure assumptions, and unless they are approximately valid for a real shallow cavity, the three-dimensional slot model we propose will be of little practical use. Indeed, for a true shallow cavity, the most appropriate value of A_{zx} to use within the slot model could well depend on the other parameters of equations (2.11)–(2.19), namely Ra_z and Bi, in addition to the actual physical cavity aspect ratio.

In spite of this difficulty, we believe that there is still value in studying the proposed slot model. The mathematical simplicity of the model means that it can be solved very rapidly on a computer, compared with a full three-dimensional simulation. Only ordinary, as opposed to partial, differential equations need to be solved. We can therefore quickly identify interesting regions of parameter space, which (as suggested earlier) can in principle be further investigated via a full simulation. Bearing in mind the comparatively large set of parameters influencing the system (Ra_z, Bi and A_{zx}) this represents a significant advantage. In the subsection that follows we give details of the numerical algorithm used to implement the model.

2.3. *Numerical implementation*

Equations (2.11)–(2.21) were solved with a shooting method. At each step nine unknowns needed to be guessed: six lower boundary conditions $u_{10,y}(0)$, $u_{01,y}(0)$, $w_{10,y}(0)$, $w_{01,y}(0)$, $T_{10}(0)$ and $T_{01}(0)$, and three pressures p_{20}, p_{02} and p_{11}. In practice two of these nine guesses were known in advance since the constant p_{20} and the function $u_{10}(y)$ always vanish in the $Pr \to \infty$ limit that we consider. With these guesses, differential equations (2.11)–(2.17) were solved via a fourth-order Runge–Kutta method (a uniform mesh of 200 points was found to be adequate here). It was then determined by how much the nine equations represented by (2.19)–(2.21) were violated (the integrals being computed by Simpson's rule). New guesses at the lower boundary and for the pressures were then obtained via the Newton–Raphson technique, and this procedure was repeated until equations (2.19)–(2.21) were satisfied within some specified tolerance. This tolerance varied between 10^{-6} and 2×10^{-4} according to the choice of other parameter values.

The Newton–Raphson technique requires the computation of a Jacobian matrix at each step. We obtained this by performing a regular perturbation expansion on the governing differential equations, i.e. we solved the linearized equations corresponding to the cases where the guessed lower boundary conditions or the pressures were subjected to arbitrarily small changes. Thus each Newton–Raphson step requires one Runge–Kutta integration of the nonlinear equations, followed by nine separate integrations of the linearized ones.

Convergence of the Newton–Raphson technique relies on good initial guesses of lower boundary conditions and pressures. This was achieved by employing known analytic forms of the solutions valid in the small-Ra_z limit which have been reported in the literature (Grassia & Homsy 1998*b*). These asymptotic analytic forms were also useful for checking that the computer program was running correctly. They were adequate starting points to ensure Newton–Raphson convergence even for Ra_z values up to the order of unity. After this Ra_z was increased in small steps, using the solution at each Ra_z value as the starting guess for the next. The target value of Ra_z was 50 000, because Rayleigh numbers are estimated to be up to tens of thousands in a bench-scale experiment under typical microgravity conditions (Richardson 1999): also see the Appendix. In addition the value $Ra_z = 50\,000$ was thought to be large enough to begin to reveal any boundary layer behaviour that might arise in the flow and/or temperature fields, which was one of the main objectives of the study.

It is also possible without loss of generality to consider positive Ra_z only. This is because the governing equations have a reflectional symmetry (Grassia & Homsy 1998*b*, *c*): if Ra_z switches sign, then so do u_{01}, w_{10}, p_{11} and T_{01}, while u_{10}, v_{00}, w_{01}, p_{00}, p_{20}, p_{02} and T_{10} remain unchanged.

3. Numerical results

Now we turn to the numerical results from the program. We shall focus on large Ra_z values, because, for small Ra_z, perturbation expansions are already known to be adequate (Grassia & Homsy 1998*b*). We concentrate on temperature profiles to the exclusion of those of velocity, since analogously to Grassia & Homsy (1998*b*), we expect the temperature fields to exhibit a richer physical behaviour. We shall identify three different regimes of behaviour which we classify according to the shape of the profile $T_{01}(y)$. The classification scheme is: T_{01} is nearly constant across the whole

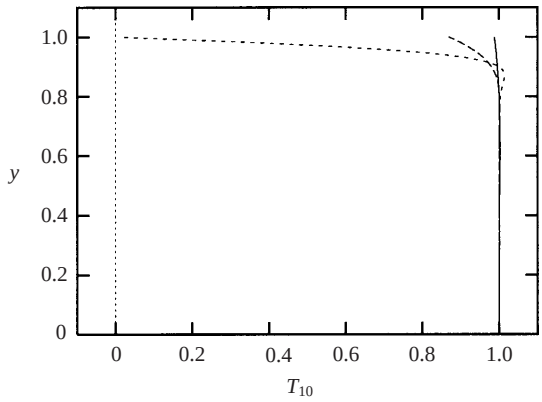

FIGURE 2. Temperature profiles T_{10} for $Ra_z = 50\,000$, $A_{zx} = 1$ and $Bi = 0.1$ (regime I, solid line), $Bi = 2$ (regime II, long dashes) and $Bi = 1000$ (regime III, short dashes). Over most of the fluid $T_{10} \approx 1$. In regimes I and II there are small departures from this near the top surface, whereas in regime III there is a large departure at that surface. These departures are a requirement of the upper thermal boundary condition.

depth (regime I), T_{01} is confined to a boundary layer near the top surface (regime II), and T_{01} is confined to a boundary layer *near* the top, but returns back to zero *at* the top (regime III). Regime selection will depend on the other two parameters of the problem: the Biot number Bi and the aspect ratio A_{zx}. Our challenge will be to determine how the magnitude of T_{01} in each regime scales with Ra_z, Bi and A_{zx}. Whenever prominent boundary layer behaviour is evident, we also wish to determine how the boundary layer thickness scales with these parameters.

Specifically, the investigation is organized as follows. Initially we fix $A_{zx} = 1$, treating three different Biot numbers in turn, $Bi = 0.1$, 2 and 1000, and investigate how the solutions depend on Ra_z. Finally we consider the effect of varying A_{zx}.

3.1. *The case* $Bi = 0.1$

The field T_{10} is shown in figure 2 assuming parameters $Ra_z = 50\,000$, $A_{zx} = 1$ and $Bi = 0.1$. Here T_{10} is nearly constant with depth, and in fact roughly equal to unity. Recall that the total lengthwise temperature gradient is made up of an applied gradient -1 and an advected gradient T_{10}. Thus under a large spanwise acceleration, the total lengthwise temperature gradient $T_{10} - 1$ almost vanishes. At high Ra_z, the slot establishes a flow and advects temperature such as to nearly cancel the applied gradient originally producing the motion. This feature will arise repeatedly in our study (recall the discussion of § 2.1).

If we look closely at figure 2, still at the $Bi = 0.1$ curve, we can see that T_{10} shows a very slight decrease over a thin layer near the top boundary. Such a decrease can be shown to be essential to satisfy the upper thermal boundary condition. This is indirect evidence of boundary layer behaviour, but it is not extremely compelling. Later we shall discover that, if the temperature decrease is achieved over a region of thickness δ_* say, then the actual amount T_{10} deviates from unity is $O(Bi\,\delta_*)$. Since Bi and δ_* are both small here, the decrease we see is likewise small.

It is a valid question to ask how this thickness δ_* scales with Ra_z. However, given that the T_{10} change near the upper surface is already so small, we were not confident that we could find a sufficiently unambiguous definition of δ_* to extract any meaningful results from our data. The striking qualitative feature of the T_{10} profile

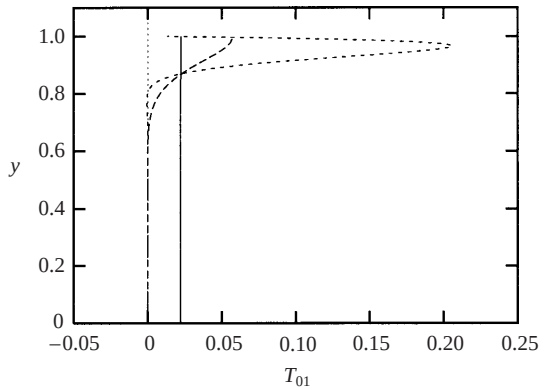

FIGURE 3. Temperature profiles T_{01} for $Ra_z = 50\,000$, $A_{zx} = 1$ and $Bi = 0.1$ (solid line), $Bi = 2$ (long dashes) and $Bi = 1000$ (short dashes). The respective curves correspond to three different regimes of behaviour: T_{01} roughly constant over the layer (regime I), T_{01} bulging in a boundary layer and finishing with a large value at the top surface (regime II), and T_{01} bulging in a boundary layer, but returning almost to zero at the top surface (regime III).

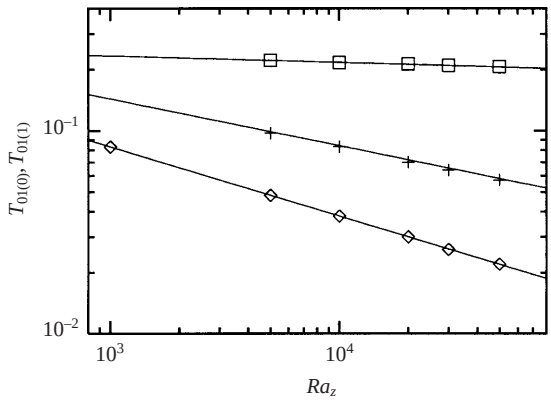

FIGURE 4. Value of $T_{01(0)}$ (regime I) or $T_{01(1)}$ (regimes II and III) vs. Ra_z for $A_{zx} = 1$ and $Bi = 0.1$ (◇), $Bi = 2$ (+), $Bi = 1000$ (□). The following power laws are observed: $T_{01(0)} \propto Ra_z^{-0.34}$ (regime I), $T_{01(1)} \propto Ra_z^{-0.23}$ (regime II) and $T_{01(1)} \propto Ra_z^{-0.032}$ (regime III). Best-fit lines through the data are shown.

seems to be the fact that it is very nearly unity, and not its small departure from this unit value. We shall see that this is in strong contrast to other regions of parameter space where boundary layer behaviour can be very readily identified.

Figure 3 shows for $Bi = 0.1$ (still with Ra_z and A_{zx} as above) that T_{01} is nearly constant across the entire layer. This type of T_{01} profile we shall take as being characteristic of our first behavioural regime, regime I. We introduce the symbol $T_{01(0)}$ to denote this uniform T_{01} value. There is no straightforward way of determining what level $T_{01(0)}$ should achieve in the large-Ra_z limit. This is in contrast to T_{10} which we have seen saturates at unity for large Ra_z, so as to cancel the applied temperature field.

In figure 4 we have plotted how $T_{01(0)}$ depends on Ra_z (log-log plot). For the purposes of this figure we have defined $T_{01(0)}$ specifically to be the maximum of T_{01} measured across the depth. Data are shown for $Ra_z = 1000$, 5000, 10 000, 20 000,

	Predicted	Numerical
Regime I		
Ra_z dependence, $T_{01(0)}$	$Ra_z^{-1/3}$	$Ra_z^{-0.34}$
δ_*	$Ra_z^{-1/3}$	Layer not prominent
A_{zx} dependence, $A_{zx} \gg 1$		
$T_{01(0)}$	$A_{zx}^{-2/3}$	$A_{zx}^{-0.71}$
δ_*	$A_{zx}^{1/3}$	Layer not prominent
A_{zx} dependence, $A_{zx} \ll 1$		
$T_{01(0)}$	$A_{zx}^{-4/3}$	$A_{zx}^{-1.27}$
δ_*	$A_{zx}^{-1/3}$	Layer not prominent
Regime II		
Ra_z dependence, $T_{01(1)}$	$Ra_z^{-1/4}$	$Ra_z^{-0.23}$
δ	$Ra_z^{-1/4}$	$Ra_z^{-0.20}$
A_{zx} dependence, $A_{zx} \gg 1$		
$T_{01(1)}$	$A_{zx}^{-3/4}$	$A_{zx}^{-0.76}$
δ	$A_{zx}^{1/4}$	$A_{zx}^{0.20}$
A_{zx} dependence, $A_{zx} \ll 1$		
$T_{01(1)}$	Independent of A_{zx}	Transitional
δ	Independent of A_{zx}	Transitional
Regime III		
Ra_z dependence, $T_{01(1)}$	Independent of Ra_z	$Ra_z^{-0.032}$
δ	$Ra_z^{-1/3}$	$Ra_z^{-0.34}$
A_{zx} dependence, $A_{zx} \gg 1$		
$T_{01(1)}$	A_{zx}^{-1}	$A_{zx}^{-0.95}$
δ	$A_{zx}^{1/3}$	$A_{zx}^{0.32}$
A_{zx} dependence, $A_{zx} \ll 1$		
$T_{01(1)}$	Independent of A_{zx}	Transitional
δ	Independent of A_{zx}	Transitional

TABLE 1. Comparison between predicted and numerically observed power-law scalings for spanwise temperature $T_{01(0)}$ or $T_{01(1)}$, and for layer thicknesses δ_* or δ. Reasonable agreement is found between prediction and numerics, except when the boundary layers thicken in regime II (δ increases) either for Ra_z of only a few thousand or for large A_{zx}. Numerical data are not reported in all cases. The boundary layers for regime I were not very prominent: they corresponded to relatively minor temperature changes, making their thickness difficult to define numerically. Also, starting from regimes II or III, reducing A_{zx} seemed to cause rapid transition to new regimes, making comparison with the predicted power-law scalings of the original regime inappropriate.

30 000 and 50 000. A best-fit line drawn through the points indicates

$$T_{01(0)} \propto Ra_z^{-0.34}. \tag{3.1}$$

For the convenience of the reader, this power law and a number of other similar ones to follow, are summarized in table 1.

Note that, unlike T_{10}, the profile T_{01} for $Bi = 0.1$ (figure 3) does not show any noticeable tendency to decrease near the top boundary. It must in fact do so, since that is a requirement of the upper thermal boundary condition. Nonetheless the decrease is evidently too slight, and confined to too small a thickness to be readily visible. Later we shall see a dramatic contrast in other regions of parameter space which exhibit a very prominent temperature decrease at the top of the profile.

3.2. *The case* $Bi = 2$

In figure 2 with $Bi = 2$ we can see that T_{10} is again unity over most of the depth of the slot, i.e. the advected field again cancels the applied field. However, there is a decrease in T_{10} near $y = 1$. The overall decrease is still rather small compared to unity, but nonetheless is much more prominent here than was the case previously for $Bi = 0.1$.

The T_{01} profile shows the most significant changes (see figure 3). It is now essentially zero over most of the depth of the slot, but bulges out near the top. This is clear boundary layer behaviour and we classify this type of profile as being regime II.

The maximum value of T_{01} in the bulge we shall denote by $T_{01(1)}$. The distinct notation $T_{01(1)}$ in place of $T_{01(0)}$ is intended as a reminder that we are now dealing with a boundary layer profile, not a constant profile. In figure 3 this maximum temperature appears to occur very close to $y = 1$. Nonetheless the upper thermal boundary condition implies it can never occur precisely at $y = 1$.

As before we have no *a priori* simple way of determining how $T_{01(1)}$ should scale with Ra_z. In figure 4 we show $T_{01(1)}$ for $Bi = 2$, $A_{zx} = 1$ and $Ra_z = 5000$, 10 000, 20 000, 30 000 and 50 000. A best-fit line indicates that

$$T_{01(1)} \propto Ra_z^{-0.23}. \tag{3.2}$$

Since we now have a very prominent boundary layer, it is natural to ask how the boundary layer thickness, denoted δ say, scales with Ra_z. The distinct notation δ, instead of δ_*, is intended as a reminder that the thickness is now measured from the T_{01} profile, not the T_{10} profile. Indeed we have chosen to define δ as the distance measured downward from the top surface at which T_{01} first falls below the value $0.001\,T_{01(1)}$. This choice is rather arbitrary, but the parametric behaviour of δ should be fairly insensitive to the precise definition, especially if T_{01} decays exponentially to zero outside the boundary layer, a model which we shall adopt later. A best-fit line, based on the same parameter values as in figure 4, suggests

$$\delta \propto Ra_z^{-0.20}. \tag{3.3}$$

Note that the δ values observed here are over half the full depth of the slot for $Ra_z \leqslant 10\,000$, and are still around a third of the depth for $Ra_z = 50\,000$. Therefore we are not strictly in a *boundary* layer regime, where ideally the boundary layer should be asymptotically very thin compared to the overall depth. Increasing Ra_z would be an effective way of making the boundary layer thinner. We have chosen not to do this in our numeric computations however, because we are unlikely to encounter Ra_z any larger than 50 000 in a typical experiment under microgravity conditions (Richardson 1999).

3.3. *The case* $Bi = 1000$

Figure 2 shows the profile for temperature T_{10} for the case $Ra_z = 50\,000$, $A_{zx} = 1$ and $Bi = 1000$. Once again this is unity over most of the depth of the slot. However, T_{10} shows a very dramatic decrease near the top boundary, falling back nearly to zero. This is a consequence of the upper thermal boundary condition. At this large Bi value, $Bi = 1000$, it is so easy for heat to escape from the top boundary that the surface temperature can remain at a value only slightly different from ambient.

The corresponding profile for T_{01} is shown in figure 3. It is again zero for most of the depth of the slot, and has a bulge in an upper boundary layer. However, the new

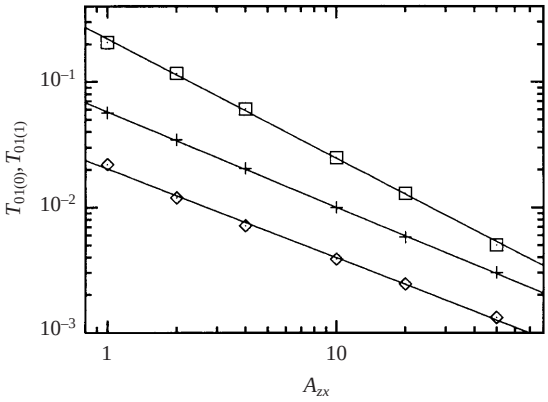

FIGURE 5. Value of $T_{01(0)}$ (regime I) or $T_{01(1)}$ (regimes II and III) vs. A_{zx} for $A_{zx} \geqslant 1$, $Ra_z = 50\,000$ and $Bi = 0.1$ ($\diamond$), $Bi = 2$ ($+$), $Bi = 1000$ ($\square$). The following power-laws are observed: $T_{01(0)} \propto A_{zx}^{-0.71}$ (regime I), $T_{01(1)} \propto A_{zx}^{-0.76}$ (regime II) and $T_{01(1)} \propto A_{zx}^{-0.95}$ (regime III). Best-fit lines through the data are shown.

feature is that T_{01} returns back to nearly zero at the upper surface, which is again a consequence of the upper thermal boundary condition. We shall call this sort of behaviour regime III.

Best-fit lines now indicate

$$T_{01(1)} \propto Ra_z^{-0.032}, \tag{3.4}$$

$$\delta \propto Ra_z^{-0.34}. \tag{3.5}$$

Observe in particular (see figure 4) that $T_{01(1)}$ is a very weak function of Ra_z.

We now summarize our numerical results thus far, corresponding to $A_{zx} = 1$. Three regimes of behaviour have been identified in the large-Ra_z limit, each characterized by the shape of the T_{01} profile: regime I has T_{01} nearly constant, regime II has T_{01} confined to a boundary layer near the top surface, and regime III has T_{01} confined to a similar layer, but with T_{01} returning back to near zero at the top surface. For completeness, one could envisage a hypothetical fourth regime in which T_{01} was constant and non-zero over most of the depth, but returned back to near zero at the upper surface: we shall discuss the possibility of such behaviour again shortly.

We have established that varying Bi is one way of selecting each of the three observed regimes. Our aim in the remainder of this section is to understand the effect of varying the spanwise-to-lengthwise aspect ratio A_{zx}.

3.4. *Varying A_{zx}: $A_{zx} \geqslant 1$*

Using the same three Bi values as before, 0.1, 2 and 1000, and keeping $Ra_z = 50\,000$, we now consider aspect ratios A_{zx} greater than unity. Aspect ratios less than unity are considered in the next subsection.

For $Bi = 0.1$, increasing A_{zx} gives no major change in the shape of the temperature profiles. In particular the temperature is still more or less uniform over height, with a value we denote $T_{01(0)}$. However the magnitude of this decreases as A_{zx} increases. In figure 5 we have plotted $T_{01(0)}$ vs. A_{zx} (log-log scale) for the values $A_{zx} = 1$, 2, 4, 10, 20 and 50. A best-fit line indicates

$$T_{01(0)} \propto A_{zx}^{-0.71}. \tag{3.6}$$

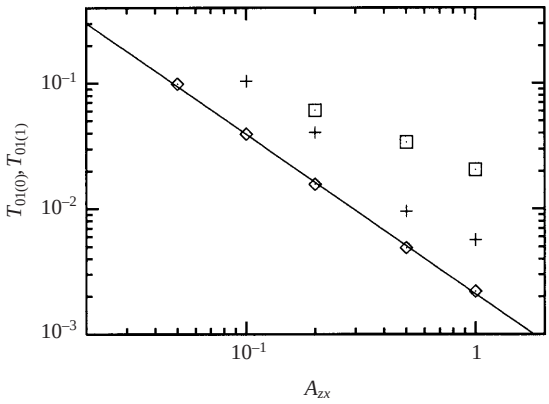

FIGURE 6. Value of $T_{01(0)}$ (regime I) or $T_{01(1)}$ (regimes II and III) vs. A_{zx} for $A_{zx} \leqslant 1$, $Ra_z = 50\,000$ and $Bi = 0.1$ ($\diamond$), $Bi = 2$ (+), $Bi = 1000$ ($\square$). The following power-law is observed for $Bi = 0.1$: $T_{01(0)} \propto A_{zx}^{-1.27}$ (regime I) and a best-fit line is shown. The $Bi = 2$ and $Bi = 1000$ data enter a transitional regime as A_{zx} decreases, suggesting it may be inappropriate to fit a power law here.

For $Bi = 2$, increasing A_{zx} has two effects. First, the temperature bulge $T_{01(1)}$ decreases. This decrease is shown in figure 5. The best-fit line is

$$T_{01(1)} \propto A_{zx}^{-0.76}. \tag{3.7}$$

The second effect is that the boundary layers become thicker. The best fit to data suggests

$$\delta \propto A_{zx}^{0.20}. \tag{3.8}$$

Equation (3.8) was determined based on A_{zx} values 2, 4, 10 and 20. The value $A_{zx} = 1$ is too small for these asymptotics to apply, while for $A_{zx} = 50$ the bulge is far too thick to be considered just a boundary layer. Presumably, for a large enough A_{zx} value, the bulge will occupy the entire slot depth, meaning that temperature is essentially uniform with depth. In other words the system will undergo a transition from regime II to regime I. We consider these transitions in more detail later.

For $Bi = 1000$ the effects of increasing A_{zx} are similar to the $Bi = 2$ case. Best-fit lines (again excluding $A_{zx} = 1$) are

$$T_{01(1)} \propto A_{zx}^{-0.95}, \tag{3.9}$$

$$\delta \propto A_{zx}^{0.32}. \tag{3.10}$$

The boundary layer bulge thickens as A_{zx} grows. We envisage that, were it to continue thickening indefinitely, we could eventually enter the hypothetical fourth regime discussed above, in which temperature is again nearly uniform with depth, but then falls back to zero at the top boundary (to satisfy the upper thermal boundary condition).

3.5. *Varying* A_{zx}: $A_{zx} \leqslant 1$

Now we consider cases where A_{zx} is decreased below unity. For $Bi = 0.1$ and $Ra_z = 50\,000$, decreasing A_{zx} gives no qualitative change in the shapes of the temperature profiles, i.e. T_{01} is still uniform with depth. Figure 6 shows how $T_{01(0)}$ changes with A_{zx} for $A_{zx} = 1$, 0.5, 0.2, 0.1 and 0.05. A best-fit line indicates

$$T_{01(0)} \propto A_{zx}^{-1.27}. \tag{3.11}$$

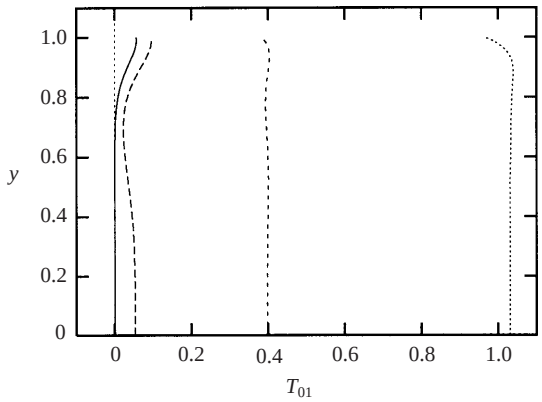

FIGURE 7. Temperature profiles T_{01} for $Ra_z = 50\,000$, $Bi = 2$, and $A_{zx} = 1$ (solid line), $A_{zx} = 0.5$ (long dashes), $A_{zx} = 0.2$ (short dashes) and $A_{zx} = 0.1$ (dots). As A_{zx} decreases, T_{01} changes shape, from being confined to a boundary layer to roughly constant across the full depth of the fluid.

Now we turn to the case $Bi = 2$ (still with $Ra_z = 50\,000$). Profiles of T_{10} remain uniform with depth and close to unity as A_{zx} decreases, but the T_{01} profiles undergo important changes. Figure 7 shows a series of T_{01} profiles for $A_{zx} = 1$, 0.5, 0.2 and 0.1. The $A_{zx} = 1$ profile is typical of regime II, with T_{01} confined to an upper boundary layer. However for $A_{zx} = 0.5$, a transition is occurring with a bulge developing at the lower boundary, in addition to the upper boundary. For $A_{zx} = 0.2$ the upper and lower bulges have merged, and T_{01} is more or less uniform with depth. This is typical of regime I. If A_{zx} decreases further to 0.1, we also have a typical regime I profile but with a larger overall temperature.

Thus it would appear that regime II exists only in a window of A_{zx} values, and that for both very small and very large aspect ratio, transitions to regime I can be induced. In figure 6 we have plotted the depth maximum T_{01} value vs. A_{zx}. For $Bi = 2$ there is a very clear change in slope between the first two and last two points, which may indicate a transition between regimes. Given that this transition is occurring, there seemed little point in determining a best-fit line.

A warning must be issued here. When we decreased A_{zx} down to 0.05 (not shown in figure 7) we moved to a completely different solution branch. On this new branch T_{01} was negative across the full depth of the slot, and was of much smaller magnitude than the profiles in figure 7. Moreover the T_{10} profiles showed a major qualitative change. Rather than T_{10} being compelled to remain near unity over the depth of the slot, it was found to vary quite significantly with depth. Despite this, the average of T_{10} over depth remained near unity. There was no evidence of boundary layer behaviour in either T_{10} or T_{01}. Both functions varied smoothly with depth and not abruptly in thin layers. We have no explanation for this qualitative change in behaviour, nor have we identified which balances in the governing equations might be responsible. Indeed our primary objective in this work has been to investigate boundary layer behaviour, and toward this end we have only proposed models (see the next section) that explain those solutions exhibiting thin layers.

When we decrease A_{zx} for $Bi = 1000$ we see similar features to the $Bi = 2$ case. In particular T_{01} profiles, shown in figure 8, develop a bottom-boundary bulge as A_{zx} decreases from 1 through 0.5 to 0.2. There might be an expectation that the two bulges would merge at small enough A_{zx}, giving a transition from regime III to our hypothetical fourth regime: uniform T_{01} over most of the depth, but falling to zero

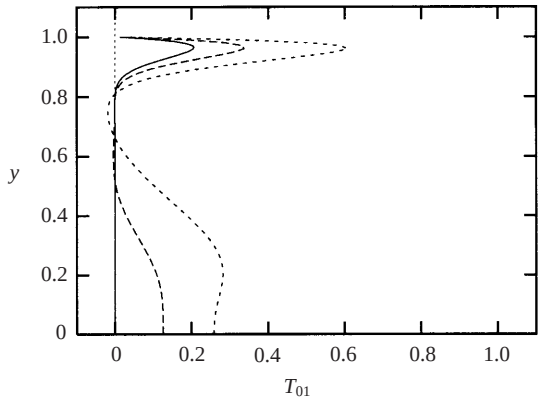

FIGURE 8. Temperature profiles T_{01} for $Ra_z = 50\,000$, $Bi = 1000$, and $A_{zx} = 1$ (solid line), $A_{zx} = 0.5$ (long dashes) and $A_{zx} = 0.2$ (short dashes). As A_{zx} decreases, T_{01} changes shape, from being confined to a boundary layer at the top surface to developing bulges at both top and bottom surfaces.

at the top. The merger is never completed however, because by $A_{zx} = 0.1$ (not shown in the figure), the system has jumped to a new solution branch, analogous to what occurred for $Bi = 2$. We can offer no explanation of this, and instead the remainder of the paper will concentrate on trying to account for regimes I, II and III.

4. The boundary layer model

The equations that have been solved numerically are complicated nonlinear differential equations with many terms. The following questions arise from this study:

Can we understand the solutions at large Ra_z in simple terms?

Can we identify the governing terms in each of the equations?

Can we explain the behaviour with respect to the parameters A_{zx} and Bi?

The obvious feature of the majority of our solutions is that they involve temperatures and/or temperature gradients confined to thin layers (boundary layers). Thus the thin-layer concept is a natural starting point in the search for a simple description. In what follows, we attempt to model this behaviour. Our models are merely approximate, but they do at least make analytic predictions of how layer thicknesses change with the governing parameters.

The algebraic manipulations needed to produce the model are quite lengthy, and may seem daunting given the large number of coupled equations. However, the general concept is a fairly simple one, and applies quite universally to any boundary layer theory. We identify the dominant balances in the equations (the choice can be justified *a posteriori* if necessary). Different terms may be in balance depending on whether we are inside or outside a boundary layer. Higher-derivative terms of course tend to be important within boundary layers, while slowly varying (non-boundary layer) functions are essentially constant within such layers. Integration across boundary layers tends to be a safe procedure since it is somewhat insensitive to the precise functional form of velocity and temperature profiles within these layers. These ideas are used repeatedly below to produce the power-law scalings we require.

4.1. *Regime I*

The numerical results identified three regimes (I, II and III) characterized by the shape of the function T_{01}. It is natural to produce a separate model for each regime.

In this subsection we address regime I. We shall discover that the lengthwise advected temperature gradients are maintained by spanwise bulk convection, and that spanwise temperature gradients are maintained by lengthwise surface convection (i.e. convection along a boundary layer).

In regime I, $T_{10} = 1$ over most of the depth of the cavity, with a very small departure near the surface, and T_{01} is nearly constant across the entire layer. Suitable approximate functions that may be used to model T_{10} and T_{01} are therefore

$$T_{10} \approx 1 - Bi\,\delta_* \exp\left(\frac{y-1}{\delta_*}\right) \quad (Bi\,\delta_* \ll 1), \tag{4.1}$$

$$T_{01} \approx T_{01(0)}, \quad \text{constant}. \tag{4.2}$$

We have used the symbol δ_*, as distinct from δ, here to denote the thickness over which T_{10} deviates from unity. This is to remind us that the function T_{01} does not exhibit any obvious boundary layer in regime I (a clear contrast with regimes II and III). It should be noted that equation (4.1) satisfies the upper thermal boundary condition to a good approximation provided the requirement $Bi\,\delta_* \ll 1$ is satisfied, i.e. provided the maximal amount that T_{10} departs from unity is small: if T_{10} falls by $O(Bi\,\delta_*)$ over a thickness $O(\delta_*)$, then $T_{10,y} = -O(Bi)$ at $y = 1$, and hence will balance BiT_{10} there. Equation (4.2) does not satisfy the upper thermal boundary condition however. The actual T_{01} must deviate from $T_{01(0)}$ at the top surface, but this deviation seems to be negligibly small.

Recall (from § 2.3) that the solution of equation (2.12) is $u_{10} = 0$. Moreover for the temperature field proposed above, $T_{01} = T_{01(0)}$, the solution of equation (2.15) is $w_{01} = 0$. It follows from equation (2.11) that $v_{00} = 0$. Hence equations (2.16)–(2.17) become

$$w_{10} T_{01} = T_{10,yy}, \tag{4.3}$$

$$u_{01}(T_{10} - 1) = T_{01,yy}. \tag{4.4}$$

Since we have assumed particular temperature fields in equations (4.1)–(4.2) thermal equations (4.3)–(4.4) are no longer satisfied exactly. However, these equations can be exploited in order-of-magnitude terms to obtain estimates for the unknowns $T_{01(0)}$ and δ_*.

We manipulate equations (4.3)–(4.4) into more convenient forms by integrating them with respect to y from 0 to 1. The left-hand side of (4.3) gives

$$\int_0^1 w_{10} T_{01}\,\mathrm{d}y \approx T_{01(0)} \int_0^1 w_{10}\,\mathrm{d}y \quad (\text{since } T_{01} \text{ is constant}). \tag{4.5}$$

The right-hand side gives

$$\begin{aligned} \int_0^1 T_{10,yy}\,\mathrm{d}y &= T_{10,y}(1) - T_{10,y}(0) \\ &= -BiT_{10}(1) \quad (\text{using the boundary conditions}) \\ &= -Bi \quad (\text{to a good order of accuracy if } Bi\,\delta_* \ll 1). \end{aligned} \tag{4.6}$$

Hence we have

$$T_{01(0)} \int_0^1 w_{10}\,\mathrm{d}y \approx -Bi. \tag{4.7}$$

An analogous integration for equation (4.4) gives on the left-hand side

$$\int_0^1 u_{01}(T_{10}-1)\,\mathrm{d}y \approx u_{01}(1)\int_0^1 (T_{10}-1)\,\mathrm{d}y \approx -u_{01}(1)Bi\,\delta_*^2, \tag{4.8}$$

where we have made use of equation (4.1) and we are assuming δ_* is small. Note that the slowly varying function u_{01} has been taken out of the integral here. The right-hand side gives

$$\begin{aligned}\int_0^1 T_{01,yy}\,\mathrm{d}y &= T_{01,y}(1) - T_{01,y}(0)\\ &= -BiT_{01}(1) \quad \text{(using the boundary conditions)}\\ &= -BiT_{01(0)} \quad \text{(since } T_{01} \text{ is constant).}\end{aligned} \tag{4.9}$$

Hence we have

$$-u_{01}(1)Bi\,\delta_*^2 \approx -BiT_{01(0)} \Rightarrow T_{01(0)} \approx u_{01}(1)\delta_*^2. \tag{4.10}$$

In the above derivation, the steps where we have replaced $T_{01,y}(1)$ by $-BiT_{01(0)}$ warrant some explanation, since it is obvious that in our model equation (4.2) the gradient $T_{01,y}$ vanishes everywhere. The actual $T_{01,y}$ must deviate from zero extremely near $y = 1$, and must roughly equal $-BiT_{01(0)}$ there (upper thermal boundary condition).

Equations (4.7) and (4.10) are a pair of simultaneous equations for $T_{01(0)}$ and δ_*. They both express the balance between horizontal convection (bulk spanwise convection across the full depth of the slot in the case of equation (4.7) and lengthwise convection confined to a surface boundary layer in equation (4.10)) and vertical conduction. The vertical conduction is associated with elevated slot temperatures, as the surface heat escape is governed by the upper thermal boundary condition (and hence by the Biot number). Differing amounts of convection at different x and z values lead to differing amounts of conduction, and hence different temperature elevations: thus x and z gradients of advected temperature are maintained. Equations (4.7) and (4.10) may be solved given $\int_0^1 w_{10}\,\mathrm{d}y$ and $u_{01}(1)$. The derivation of $\int_0^1 w_{10}\,\mathrm{d}y$ and $u_{01}(1)$ will now be described and the consequent power laws for $T_{01(0)}$ and δ_* appear immediately after that.

4.1.1. *Calculation of* $\int_0^1 w_{10}\,\mathrm{d}y$ *and* $u_{01}(1)$

The quantities $\int_0^1 w_{10}\,\mathrm{d}y$ and $u_{01}(1)$ may be found via equations (2.13), (2.14) and (2.20). Solving (2.13) is straightforward as p_{11} in the equation is just a constant. Solving for w_{10} is slightly more complicated. Equation (2.14) becomes

$$w_{10,yy} = p_{11} - Ra_z(T_{10}-1). \tag{4.11}$$

The second term on the right-hand side is confined to a boundary layer of thickness $O(\delta_*)$ at the top surface, and we anticipate that it completely dominates p_{11} there. We integrate equation (4.11) across the layer to determine $w_{10,y}$ at a point immediately below the layer (we denote this point by $y = 1^-$). We find using equation (4.1)

$$w_{10,y}(1^-) = -Ra_z\,Bi\,\delta_*^2. \tag{4.12}$$

We can now solve $w_{10,yy} = p_{11}$ which applies outside the boundary layer and substitute the expressions for u_{01} and w_{10} into (2.20), and then solve to obtain

$$u_{01}(1) = \frac{3}{4}\frac{Ra_z\, Bi\, \delta_*^2}{(1 + A_{zx}^2)}, \tag{4.13}$$

$$\int_0^1 w_{10}\, \mathrm{d}y = -\frac{Ra_z\, Bi\, \delta_*^2\, A_{zx}^2}{2(1 + A_{zx}^2)}, \tag{4.14}$$

which are the quantities we require.

4.1.2. *Prediction of power-law behaviour of $T_{01(0)}$ and δ_**

Substituting results (4.13) and (4.14) into equations (4.7) and (4.10), solving the last two equations simultaneously, and discarding all $O(1)$ factors (we are interested in extracting power laws only), we deduce

$$T_{01(0)} \propto Ra_z^{-1/3} Bi^{1/3} \frac{(1 + A_{zx}^2)^{1/3}}{A_{zx}^{4/3}}, \tag{4.15}$$

$$\delta_* \propto Ra_z^{-1/3} Bi^{-1/6} \left(\frac{1 + A_{zx}^2}{A_{zx}}\right)^{1/3}. \tag{4.16}$$

These predicted power laws (and others to follow) are tabulated alongside the numerically observed ones in table 1.

4.2. *Regime II*

Now we turn to regime II. As before $T_{10} = 1$ over most of the depth of the cavity, with a small departure near the surface. However, now $T_{01} = 0$ over the lower part of the cavity with a significant bulge near the surface. The maximum value of T_{01} is denoted by $T_{01(1)}$, and this occurs extremely close to the top surface. The thickness of the region where T_{10} deviates from unity and the thickness of the bulge in T_{01} are roughly the same. Hence we may use the following models for T_{10} and T_{01}:

$$T_{10} \approx 1 - Bi\, \delta \exp\left(\frac{y - 1}{\delta}\right) \quad (Bi\, \delta \ll 1), \tag{4.17}$$

$$T_{01} \approx T_{01(1)} \exp\left(\frac{y - 1}{\delta}\right). \tag{4.18}$$

Again (4.17) satisfies the upper thermal boundary condition (provided $Bi\, \delta \ll 1$), while (4.18) does not. However, it appears that the deviation away from (4.18) is negligible and confined extremely close to the top boundary.

Physically we shall see that the mechanism producing the field T_{10} is broadly similar to that in regime I, but the mechanism for the field T_{01} is quite different, being convectively controlled. As before, thermal equations (2.16)–(2.17) are no longer satisfied in detail, but we still wish to use them (integrated from 0 to 1) to obtain the scaling laws for the unknowns $T_{01(1)}$ and δ. After some substitutions from continuity equation (2.11) and from boundary and integral conditions (2.18)–(2.21), we deduce

$$\int_0^1 w_{01}(T_{10} - 1)\, \mathrm{d}y + \int_0^1 w_{10} T_{01}\, \mathrm{d}y = T_{10,y}(1), \tag{4.19}$$

$$\int_0^1 u_{01}(T_{10} - 1)\, \mathrm{d}y + 2\int_0^1 w_{01} T_{01}\, \mathrm{d}y = T_{01,y}(1). \tag{4.20}$$

Taking the slowly varying functions out of the integrands on the left-hand side, applying the thermal boundary conditions on the right-hand side, substituting from (4.17)–(4.18) and assuming δ is small, we have

$$w_{01}(1)(-Bi\,\delta^2) + w_{10}(1)T_{01(1)}\delta \approx -Bi, \tag{4.21}$$

$$u_{01}(1)(-Bi\,\delta^2) + 2w_{01}(1)T_{01(1)}\delta \approx -BiT_{01(1)}. \tag{4.22}$$

A numerical investigation was carried out to determine the relative importance of the terms in equations (4.21) and (4.22). The investigation showed that the two terms on the left-hand side of (4.21) have the same sign and the same order of magnitude. It also showed that the two terms on the left-hand side of (4.22) have opposite sign and that the term on the right-hand side is smaller in magnitude. Therefore we may assume a balance between the terms on the left-hand side of (4.22). Hence we obtain in order-of-magnitude terms

$$2w_{10}(1)T_{01(1)}\delta \approx -Bi, \tag{4.23}$$

$$2w_{01}(1)T_{01(1)} \approx u_{01}(1)Bi\,\delta. \tag{4.24}$$

The difference between equation (4.23) here and equation (4.7) (regime I) is due solely to the convection now being confined to a boundary layer instead of being spread over the full depth of the slot. However, equation (4.24) is physically quite different from equation (4.10) (regime I): it expresses a balance between lengthwise and spanwise convection, not a conductive–convective balance which was the case before.

Equations (4.23) and (4.24) are a pair of equations for $T_{01(1)}$ and δ, given values for $w_{01}(1)$, $w_{10}(1)$ and $u_{01}(1)$. The formula for $u_{01}(1)$ given in § 4.1.1 still applies here. A formula for $w_{10}(1)$ can also be obtained via the arguments of that subsection. We find

$$w_{10}(1) = -\frac{(\frac{1}{4} + A_{zx}^2)}{(1 + A_{zx}^2)} Ra_z\, Bi\,\delta^2. \tag{4.25}$$

It remains to determine $w_{01}(1)$ and then the resulting power-law scalings for $T_{01(1)}$ and δ can be determined.

4.2.1. *Calculation of* $w_{01}(1)$

Rearranging equation (2.15) gives

$$w_{01,yy} = p_{02} - Ra_z\, T_{01}. \tag{4.26}$$

The term $-Ra_z T_{01}$ is confined to a boundary layer at the top surface, and is expected to be the dominant term there. Then, using arguments analogous to those of § 4.1.1 and applying return flow condition (2.21), we can show

$$w_{01}(1) = \tfrac{1}{4} Ra_z\, T_{01(1)}\delta. \tag{4.27}$$

4.2.2. *Prediction of power-law behaviour of* $T_{01(1)}$ *and* δ

Substituting the results from (4.13), (4.25) and (4.27) into equations (4.23) and (4.24), and also noting that the ratio $(\frac{1}{4} + A_{zx}^2)/(1 + A_{zx}^2)$ in equation (4.25) remains $O(1)$ for all A_{zx}, we arrive at the following power laws for regime II:

$$T_{01(1)} \propto Ra_z^{-1/4} Bi^{3/4} (1 + A_{zx}^2)^{-3/8}, \tag{4.28}$$

$$\delta \propto Ra_z^{-1/4} Bi^{-1/4} (1 + A_{zx}^2)^{1/8}. \tag{4.29}$$

With these scalings we can show that neglect of the right-hand side of (4.22) is self-consistent provided $Bi\,\delta \ll 1$.

4.3. *Regime III*

Next we turn to the case of regime III. Here $T_{10} = 1$ in the lower part of the cavity but $T_{10} \approx 0$ at the surface of the fluid. The value of T_{01} is approximately zero in the lower part of the cavity but in the boundary layer there is a bulge in T_{01}, with a return almost to zero at the surface. Suitable models for T_{10} and T_{01} are therefore

$$T_{10} \approx 1 - \exp\left(\frac{y-1}{\delta}\right), \tag{4.30}$$

$$T_{01} \approx T_{01(1)} \left(\frac{1-y}{\delta}\right) \exp\left(\frac{y-1}{\delta}\right) \exp(1). \tag{4.31}$$

Here $T_{01(1)}$ represents the maximum of T_{01} within the bulge, and $\exp(1)$ is a factor included for convenience because the bulge is maximal at $y = 1 - \delta$.

Proceeding as in regime II we find that equations (4.19)–(4.20) still apply. However, in place of equations (4.21)–(4.22), we find

$$-w_{01}(1)\delta + w_{10}(1)\delta\, T_{01(1)} \exp(1) \approx -\frac{1}{\delta}, \tag{4.32}$$

$$-u_{01}(1)\delta + 2w_{01}(1)\delta\, T_{01(1)} \exp(1) \approx -\frac{T_{01(1)} \exp(1)}{\delta}. \tag{4.33}$$

The last two equations may be solved for $T_{01(1)}$ and δ given values for $w_{01}(1)$, $w_{10}(1)$ and $u_{01}(1)$ from (2.13)–(2.15). In each of equations (4.32) and (4.33), the two left-hand-side terms can be shown to have the same magnitude and sign and so, in the interests of an order-of-magnitude theory, the terms involving $w_{01}(1)$ may be neglected. This is a result which may also be justified *a posteriori*. We are thus left with conductive–convective balances in both cases,

$$w_{10}(1)\delta\, T_{01(1)} \exp(1) \approx -\frac{1}{\delta}, \tag{4.34}$$

$$-u_{01}(1)\delta \approx -\frac{T_{01(1)} \exp(1)}{\delta} \Rightarrow T_{01(1)} \approx \frac{u_{01}(1)\delta^2}{\exp(1)}. \tag{4.35}$$

The difference between equation (4.34) and equation (4.23) (regime II) is explained by the changing amount of vertical conduction in the T_{10} profile, i.e. T_{10} now returning nearly to zero at the surface for large Bi, a requirement of the upper thermal boundary condition. However, equation (4.35) is quite analogous to equation (4.10) (regime I).

Proceeding with our analysis, equations (2.13)–(2.14) may be solved using similar arguments to those of the previous sections, giving ultimately

$$u_{01}(1) = \frac{3}{4} \frac{1}{(1 + A_{zx}^2)} Ra_z \delta, \tag{4.36}$$

$$w_{01}(1) = -\left(\frac{\frac{1}{4} + A_{zx}^2}{1 + A_{zx}^2}\right) Ra_z \delta, \tag{4.37}$$

instead of equations (4.13) and (4.25).

Substituting into equations (4.34)–(4.35), rearranging and discarding all $O(1)$ factors, we deduce

$$T_{01(1)} \propto (1 + A_{zx}^2)^{-1/2}, \quad \text{independent of } Ra_z, \tag{4.38}$$

$$\delta \propto Ra_z^{-1/3}(1 + A_{zx}^2)^{1/6}. \tag{4.39}$$

4.4. *Hypothetical fourth regime*

It is possible to envisage a hypothetical fourth regime in which T_{10} and T_{01} have respective values 1 and $T_{01(0)}$ away from the top boundary, and where these fall back to near zero over some thickness, δ_* say, at the top boundary. Numerical evidence for this regime is not overwhelming, but there is some suggestion it could exist for large enough Bi and extreme values of aspect ratio A_{zx}. Suitable models are

$$T_{10} \approx 1 - \exp\left(\frac{y-1}{\delta_*}\right), \tag{4.40}$$

$$T_{01} \approx T_{01(0)}\left(1 - \exp\left(\frac{y-1}{\delta_*}\right)\right). \tag{4.41}$$

Analogous to equations (4.7) and (4.10) we can derive

$$T_{01(0)} \int_0^1 w_{10}(y)\,\mathrm{d}y \approx -\frac{1}{\delta_*}, \tag{4.42}$$

$$T_{01(0)} \approx u_{01}(1)\delta_*^2, \tag{4.43}$$

and analogous to equations (4.13)–(4.14) we can derive

$$u_{01}(1) = \frac{3}{4}\frac{Ra_z\delta_*}{(1 + A_{zx}^2)}, \tag{4.44}$$

$$\int_0^1 w_{10}(y)\,\mathrm{d}y = -\frac{Ra_z\delta_* A_{zx}^2}{2(1 + A_{zx}^2)}. \tag{4.45}$$

Solving the above we deduce

$$T_{01(0)} \propto Ra_z^{-1/5}\frac{(1 + A_{zx}^2)^{1/5}}{A_{zx}^{6/5}}, \tag{4.46}$$

$$\delta_* \propto Ra_z^{-2/5}\frac{(1 + A_{zx}^2)^{2/5}}{A_{zx}^{2/5}}. \tag{4.47}$$

The physics of equations (4.42)–(4.43) is little different from that of equations (4.34)–(4.35) (regime III), except that in equation (4.42) the convective effect is now spread over the entire depth of the slot, not confined in a surface boundary layer.

5. Discussion

It is appropriate to ask how well the predictions of the model (§4) agree with the numerical data (§3). The extent of agreement is summarized in table 1. As we can see, in almost all cases for which we have data, agreement between the models and the numerical results is good. The only exceptions are the predictions of boundary layer thickness δ in regime II. This disagreement may be due to our slightly arbitrary way of defining δ, or it may just be due to the fact that the boundary layers are

becoming very thick either for Ra_z of only a few thousand or in the large-A_{zx} limit. Models which assume asymptotically thin boundary layers ($\delta \ll 1$) are therefore inappropriate. Additionally the model for regime II assumes $Bi\,\delta \ll 1$, but with $Bi = 2$ in our data this condition is certainly not satisfied. If we decided to determine a best-fit line based solely on those points with $Ra_z \geqslant 20\,000$, i.e. based on those points for which $Bi\,\delta$ is less than unity in the numerics, we would obtain rather better agreement with our prediction.

A significant achievement would be to understand which parameter value gives solutions in which regime, and how to induce transitions between the regimes. The transition between regimes II and III is quite straightforward, and is driven by the need to continue satisfying the upper thermal boundary condition as $Bi\,\delta$ ranges from values much less than one to values much greater than one. Decreasing Bi will therefore shift the slot from regime III to regime II. It is also possible in principle to drive the same transition by increasing Ra_z, since that will make the boundary layer thinner (smaller δ). However, this is unlikely to be very successful, because δ is quite a weak function of Ra_z (proportional to $Ra_z^{-1/4}$ in regime II, and $Ra_z^{-1/3}$ in regime III). Indeed we have seen in our numerical data that the boundary layers remain quite thick even for $Ra_z = 50\,000$, and under microgravity conditions we are unlikely to encounter Rayleigh numbers much bigger than that (Richardson 1999).

The transition between regime I and regime II is less obvious. It is associated with the velocity field w_{01} becoming prominent in regime II, allowing two convective terms to balance (one lengthwise, one spanwise) in the equation for T_{01}, as opposed to a conductive–convective balance which is typical of regime I (see §§ 4.1–4.2).

A simple heuristic criterion for locating the point of transition between these two regimes can be derived as follows. Think of a general T_{01} profile as being composed of a uniform background value $T_{01(0)}$ and a boundary layer bulge of temperature $T_{01(1)}$ over and above the background. The slot is in regime I or regime II according to whether the background temperature is larger or smaller than the bulge. Thus our criterion for transition between these regimes is

$$T_{01(0)} \approx T_{01(1)}, \tag{5.1}$$

with the required formulae given in equations (4.15) and (4.28). We have chosen to base our transition criterion on the model predicted temperatures $T_{01(0)}$ and $T_{01(1)}$ and not on some other system property (like δ_* or δ), because the temperature predictions seemed to show rather better agreement with the numerical results.

As $T_{01(0)} \propto Ra_z^{-1/3}$ and $T_{01(1)} \propto Ra_z^{-1/4}$, we deduce that for large enough Rayleigh number, regime II should always dominate. However, for Ra_z up to 50 000, the difference between $Ra_z^{-1/3}$ and $Ra_z^{-1/4}$ will not be very great. Hence it is instructive to determine how $T_{01(0)}$ and $T_{01(1)}$ depend on the other parameters of the slot, Bi and A_{zx}.

Consider first $O(1)$ values of A_{zx}. As $T_{01(0)} \propto Bi^{1/3}$ and $T_{01(1)} \propto Bi^{3/4}$, it is apparent that regime I will be favoured at small Bi. Indeed we can determine from equation (5.1) that the transition between the two regimes will occur when

$$Bi = O(Ra_z^{-1/5}), \tag{5.2}$$

which is certainly consistent with our numerical data. Incidentally the $Bi \ll 1$ asymptotic behaviour of the slot can now be extracted from equations (4.2)–(4.3), provided $Ra_z \gg 1$ is also large enough to ensure the regime I scaling applies.

Now consider A_{zx} values very different from unity. If $A_{zx} \gg 1$, the respective

behaviours of $T_{01(0)}$ and $T_{01(1)}$ are $A_{zx}^{-2/3}$ and $A_{zx}^{-3/4}$, making regime I dominant. If $A_{zx} \ll 1$, the respective behaviours are $T_{01(0)} \propto A_{zx}^{-4/3}$ and $T_{01(1)}$ independent of A_{zx}. Again regime I is dominant. Regime II will only exist in a window of A_{zx} values

$$O((Ra_z Bi^5)^{-1/16}) \leqslant A_{zx} \leqslant O(Ra_z Bi^5). \tag{5.3}$$

Note that $Ra_z Bi^5$ must be greater than unity for this window to exist.

Some comments are pertinent. The transition will be quite gradual for A_{zx} in excess of unity, i.e. exceedingly large A_{zx} values need be to reached before seeing any transition. However, it will be more abrupt for A_{zx} less than unity, since $(Ra_z Bi^5)^{-1/16}$ will never be extremely small. This is in agreement with our numerical results. Our numerics suggest that transition occurs by gradual thickening of the boundary layer for $A_{zx} \geqslant 1$, but by development of an additional bulge at the lower boundary which grows and merges with the upper bulge when $A_{zx} \leqslant 1$. We also recall that for very small A_{zx} values, the slot system seems to jump to a completely different solution branch. We can offer no explanation of this last phenomenon.

We would also like to understand how regime III might undergo transition, say into the hypothetical fourth regime. The physical difference between these two regimes is due to the changing nature of one of the convective terms in the T_{10} equation (see §§ 4.3–4.4): convection is confined near the upper surface of the slot in one case, but spread over the entire slot depth in the other. We again employ the criterion (5.1), taking the required formulae from (4.38) and (4.46): regime III is expected to be dominant for large Ra_z. Moreover, by comparing the expected A_{zx} dependences, we can predict that regime III should only be observed in a window of values

$$O(Ra_z^{-1/6}) \leqslant A_{zx} \leqslant O(Ra_z), \tag{5.4}$$

with the hypothetical fourth regime on either side of this window. Based on the above discussion and our numerical results, many analogies are predicted with the regime II to regime I transition. For instance, the $A_{zx} \gg 1$ transition will be gradual, and will proceed by boundary layer thickening. The $A_{zx} \ll 1$ transition should be more abrupt, and seems to involve a bottom boundary bulge. Again there seems to be a jump to an entirely different solution branch for very small A_{zx}, and we can offer no explanation for this.

6. Conclusions

In summary, for a buoyant slot subject to low-frequency, spanwise g-jitter, with a large instantaneous Rayleigh number $Ra_z \gg 1$, we have identified numerically three clear parameter regimes, along with a hypothetical fourth regime, for which there is some limited evidence. The different regimes are selected according to the values of the Biot number Bi and an aspect ratio parameter A_{zx}, and are characterized by differently shaped temperature profiles. In order to account for the numerical observations, some models have been proposed which identify the dominant physical balances in the equations. The models broadly reproduce the numerically observed scaling behaviour in each regime, and seem to predict the correct transitions between regimes. Many of our models involve boundary layers, but these do not necessarily obey the $Ra_z^{-1/4}$ scaling for layer thickness which is conventional in free-convection problems. The reason is that the conventional picture relies on a fixed temperature change applied across the layer, but we have a much more complicated system with multiple flow and advected temperature fields mutually interacting.

D. Richardson acknowledges financial support from the EPSRC.

Appendix

Here we give the relationship between dimensionless and dimensional variables. In dimensional variables we envisage a slot of depth d, containing a fluid of density ρ, kinematic viscosity ν, thermal diffusivity κ, thermal conductivity k, and thermal expansion coefficient α. There is a temperature gradient applied along the slot, such that over each distance d the temperature falls by ΔT. The top surface of the slot is characterized by a heat transfer coefficient h. The applied spanwise acceleration is g_z. Lengths are made dimensionless on the scale d, velocities on the scale κ/d, pressures on the scale $\rho\nu\kappa/d^2$, and temperatures on the scale ΔT. The Rayleigh, Prandtl and Biot numbers are defined as

$$Ra_z = \frac{\alpha \Delta T g_z d^3}{\nu\kappa}, \quad Pr = \frac{\nu}{\kappa}, \quad Bi = \frac{hd}{k}.$$

We have stated a number of times in the text that $Ra_z = 50\,000$ is a typical upper limit (Richardson 1999) for bench-scale experiments under microgravity conditions. This is based on plausible values $d = 0.1\,\mathrm{m}$ and $\Delta T = 10\,\mathrm{K}$, along with a jitter strength $g_z = 3.5 \times 10^{-3}\,\mathrm{m\,s^{-2}}$ (Thompson *et al.* 1996), and properties of water, $\alpha = 2 \times 10^{-4}\,\mathrm{K^{-1}}$, $\nu = 10^{-6}\,\mathrm{m^2\,s^{-1}}$, and $\kappa = 1.4 \times 10^{-7}\,\mathrm{m^2\,s^{-1}}$ (Batchelor 1967).

REFERENCES

Alexander, J. I. D. 1990 Low gravity experiment sensitivity to residual acceleration: A review. *Microgravity Sci. Technol.* **3**, 52–68.

Alexander, J. I. D., Lizée, A., Favier, J.-J. & Garandet, J.-P. 1996 Analysis of residual acceleration effects on transport and segregation during directional solidification of tin-bismuth in the MEPHISTO furnace facility. In *Third Microgravity Fluid Physics Conference, NASA CP*, vol. 3338, pp. 461–464.

Batchelor, G. K. 1967 *An Introduction to Fluid Dynamics.* Cambridge University Press.

Bergholz, R. F. 1978 Stability of natural convection in a vertical fluid layer. *J. Fluid Mech.* **84**, 743–768.

Biringen, S. & Danabasoglu, G. 1989 Oscillatory flow with heat transfer in a square cavity. *Phys. Fluids* A **1**, 1796–1812.

Biringen, S. & Danabasoglu, G. 1990 Computation of convective flow with gravity modulation in rectangular cavities. *J. Thermophys. Heat Transfer* **4**, 357–365.

Biringen, S. & Peltier, L. J. 1990 Numerical simulation of 3-d Bénard convection with gravitational modulation. *Phys. Fluids* A **2**, 754–764.

Braunsfurth, M. G. & Mullin, T. 1996 An experimental study of oscillatory convection in liquid gallium. *J. Fluid Mech.* **327**, 199–219.

Braunsfurth, M. G., Skeldon, A. C., Juel, A., Mullin, T. & Riley, D. S. 1997 Free convection in liquid gallium. *J. Fluid Mech.* **342**, 295–314.

Chen, W. Y. & Chen, C. F. 1999 Effect of gravity modulation on the stability of convection in a vertical slot. *J. Fluid Mech.* **395**, 327–344.

Christov, C. I. & Homsy, G. M. 2001 Nonlinear dynamics of two-dimensional convection in a vertically stratified slot with and without gravity modulation. *J. Fluid Mech.* **430**, 335–360.

Elder, J. W. 1965 Laminar free convection in a vertical slot. *J. Fluid Mech.* **23**, 77–98.

Farooq, A. & Homsy, G. M. 1994 Streaming flows due to g-jitter-induced natural convection. *J. Fluid Mech.* **271**, 351–378.

Farooq, A. & Homsy, G. M. 1996 Linear and non-linear dynamics of a differentially heated slot under gravity modulation. *J. Fluid Mech.* **313**, 1–38.

Gershuni, G. Z. & Zhukhovitskiy, Y. M. 1986 Vibration-induced thermal convection in weightlessness. *Fluid Mech. – Sov. Res.* **15**, 63–84.

Gershuni, G. Z., Zhukhovitsky, E. M., Kolesnikov, A. K. & Yurkov, Y. S. 1989 Vibrational convection in a horizontal fluid layer with internal heat sources. *Intl J. Heat Mass Transfer* **32**, 2319–2328.

Gill, A. E. 1966 The boundary layer regime for convection in a rectangular cavity. *J. Fluid Mech.* **26**, 515–536.

Gill, A. E. & Davey, A. 1969 Instabilities of a buoyancy-driven system. *J. Fluid Mech.* **35**, 775–798.

Gill, A. E. & Kirkham, C. C. 1970 A note on the stability of convection in a vertical slot. *J. Fluid Mech.* **42**, 125–127.

Grassia, P. & Homsy, G. M. 1998*a* Thermocapillary and buoyant flows with low frequency jitter. I. Jitter confined to the plane. *Phys. Fluids* **10**, 1273–1290.

Grassia, P. & Homsy, G. M. 1998*b* Thermocapillary and buoyant flows with low frequency jitter. II. Spanwise jitter. *Phys. Fluids* **10**, 1291–1314.

Grassia, P. & Homsy, G. M. 1998*c* Buoyant flows with low frequency jitter. *Phys. Fluids* **10**, 1903–1923.

Gresho, P. M. & Sani, R. L. 1970 The effects of gravity modulation on the stability of a heated fluid layer. *J. Fluid Mech.* **40**, 783–806.

Kamotani, Y., Prasad, A. & Ostrach, S. 1981 Thermal convection in an enclosure due to vibrations aboard spacecraft. *AIAA J.* **19**, 511–516.

Kondos, P. A. & Subramanian, R. S. 1996 Buoyant flow in a two-dimensional cavity due to a sinusoidal gravitational field. *Microgravity Sci. Technol.* **9**, 143–151.

Leal, L. G. 1992 *Laminar Flow and Convective Transport Processes: Scaling Principles and Asymptotic Analysis.* Butterworth–Heinemann.

Lizée, A. & Alexander, J. I. D. 1997 Chaotic thermovibrational flow in a laterally heated cavity. *Phys. Rev.* E **56**, 4152–4156.

Neitzel, G. P., Chang, K. T., Jankowski, D. F. & Mittelmann, H. D. 1993 Linear-stability theory of thermocapillary convection in a model of the float-zone crystal-growth process. *Phys. Fluids* A **5**, 108–114.

Neitzel, G. P., Law, C. C., Jankowski, D. F. & Mittelman, H. D. 1991 Energy stability of thermocapillary convection in a model of the float-zone crystal-growth process. II. Nonaxisymmetric disturbances. *Phys. Fluids* A **3**, 2841–2846.

Nelson, E. S. 1991 An examination of anticipated *g*-jitter on a space station and its effects on materials processing. *NASA Tech. Mem.* 103775.

Or, A. C. & Kelly, R. E. 1998 Thermocapillary and oscillatory-shear instabilities in a layer of liquid with a deformable surface. *J. Fluid Mech.* **360**, 21–39.

Ostrach, S. 1982 Low-gravity fluid flows. *Annu. Rev. Fluid Mech.* **14**, 313–345.

Richardson, D. 1999 Buoyant flows with strong spanwise *g*-jitter. Master's thesis, University of Manchester.

Saunders, B. V., Murray, B. T., McFadden, G. B., Coriell, S. R. & Wheeler, A. A. 1992 The effect of gravity modulation on thermosolutal convection in an infinite layer of fluid. *Phys. Fluids* A **4**, 1176–1189.

Sen, A. K. & Davis, S. H. 1982 Steady thermocapillary flows in two-dimensional slots. *J. Fluid Mech.* **121**, 163–186.

Shen, Y., Neitzel, G. P., Jankowski, D. F. & Mittelmann, H. D. 1990 Energy stability of thermocapillary convection in a model of the float-zone crystal-growth process. *J. Fluid Mech.* **217**, 639–660.

Skarda, J. R. L. 2001 Instability of a gravity-modulated fluid layer with surface tension variation. *J. Fluid Mech.* **434**, 243–271.

Smith, M. K. & Davis, S. H. 1983*a* Instabilities of dynamic thermocapillary liquid layers. Part 1. Convective instabilities. *J. Fluid Mech.* **132**, 119–144.

Smith, M. K. & Davis, S. H. 1983*b* Instabilities of dynamic thermocapillary liquid layers. Part 2. Surface-wave instabilities. *J. Fluid Mech.* **132**, 145–162.

Suresh, V. A., Christov, C. I. & Homsy, G. M. 1999 Resonant thermocapillary and buoyant flows with finite frequency gravity modulation. *Phys. Fluids* **11**, 2565–2576.

Thévenard, D. & Ben Hadid, H. 1991 Low Prandtl number convection in a rectangular cavity with longitudinal thermal gradient and transverse *g*-jitters. *Intl J. Heat Mass Transfer* **34**, 2167–2173.

Thomson, J. R., Drolet, F. & Viñals, J. 1996 Fluid physics in a fluctuating acceleration environment. In *Third Microgravity Fluid Physics Conference, NASA CP*, vol. 3338, pp. 429–434.

Wadih, M. & Roux, B. 1988 Natural convection in a long vertical cylinder under gravity modulation. *J. Fluid Mech.* **193**, 391–415.